CrossMark

A Search for Additional Bodies in the GJ 1132 Planetary System from 21 Ground-based Transits and a 100-hr *Spitzer* Campaign

Jason A. Dittmann[1] , Jonathan M. Irwin[1], David Charbonneau[1] , Zachory K. Berta-Thompson[2], and Elisabeth R. Newton[3,4]
[1] Harvard-Smithsonian Center for Astrophysics, 60 Garden Street, Cambridge, MA 02138, USA; Jason.Dittmann@gmail.com
[2] University of Colorado, 391 UCB, 2000 Colorado Avenue, Boulder, CO 80305, USA
[3] Massachusetts Institute of Technology, 77 Massachusetts Avenue, Cambridge, MA 02139, USA

Abstract

We present the results of a search for additional bodies in the GJ 1132 system through two methods: photometric transits and transit timing variations of GJ 1132b. We collected 21 transit observations of GJ 1132b with the MEarth-South array. We obtained 100 near-continuous hours of observations with the *Spitzer Space Telescope*, including two transits of GJ 1132b and spanning 60% of the orbital phase of the maximum (6.9-day) period at which bodies coplanar with GJ 1132b would transit. We exclude transits of additional Mars-sized bodies, such as a second planet or a moon, with a confidence of 99.7%. We find that the planet-to-star radius ratio inferred from the MEarth and *Spitzer* light curves are discrepant at the 3.7σ level, which we ascribe to the effects of starspots and faculae. When we combine the mass estimate of the star (obtained from its parallax and apparent K_s band magnitude) with the stellar density inferred from our high-cadence *Spitzer* light curve (assuming zero eccentricity), we measure the stellar radius of GJ 1132 to be $0.2105^{+0.0102}_{-0.0085} R_\odot$, and we refine the radius measurement of GJ 1132b to $1.130 \pm 0.056 R_\oplus$. Combined with HARPS RV measurements, we determine the density of GJ 1132b to be 6.2 ± 2.0 g cm^{-3}. We refine the ephemeris of the system (improving the period determination by an order of magnitude) and find no evidence for transit timing variations, which would be expected if there was a second planet near an orbital resonance with GJ 1132b.

Key words: eclipses – planets and satellites: individual (GJ 1132b) – stars: individual (GJ 1132) – stars: low-mass

Supporting material: machine-readable table

1. Introduction

M Dwarfs (0.08 $M_\odot < M < 0.60 M_\odot$) make up approximately 75% of the stellar population in the Milky Way (Henry et al. 2006) and are estimated to host planets similar in size to the Earth (0.5 $R_\oplus < R_p < 1.5 R_\oplus$) at a rate of approximately 1.4 planets per star (Dressing & Charbonneau 2015). Planets smaller than 1.6 $R_\oplus$ are likely to be primarily composed of rocky terrestrial material (Dressing et al. 2015; Rogers 2015). Some planets in this size range appear to have significant gaseous envelopes (Kipping et al. 2014), while some larger planets can be terrestrial in nature (Buchhave et al. 2016), indicating that size may not fully dictate the compositions of planets, and detailed characterization work is required to fully understand their natures.

The characterization of planets orbiting M dwarfs by the methods of radial velocity and transit techniques is significantly easier than characterizing planets around larger and hotter stars due to the relative sizes and masses of the star and planet. Habitable planets orbiting M dwarfs have shorter orbital periods, making them easier to discover and observe. While the *Kepler* and *K*2 missions have uncovered thousands of extrasolar planets, they operate only on 4.4% of the total area on the sky (assuming 17 observing fields for *K2*), and therefore are not surveying the majority of the closest brightest M dwarfs, which are distributed uniformly on the sky.

A new generation of surveys are using robotic arrays of multiple telescopes to survey the closest mid-to-late M dwarfs for transiting planets. Exoplanet transit surveys like MEarth (Nutzman & Charbonneau 2008; Irwin et al. 2015), TRAPPIST

(Gillon et al. 2011), and APACHE (Sozzetti et al. 2014) are currently targeting individual, nearby stars. In the near future, additional surveys like ExTrA (Bonfils et al. 2015) will come online and also target the nearby M dwarfs. The small size and cool temperatures of these stars allow ground-based surveys like MEarth to potentially be sensitive to planets in the habitable zone (Berta et al. 2012b) and for instruments like the *Hubble Space Telescope* (*HST*) and the *James Webb Space Telescope* (*JWST*) to potentially characterize their atmospheres (Berta et al. 2012a; Schwieterman et al. 2016). TRAPPIST (Gillon et al. 2011) found three transiting planets orbiting a 0.08 $M_\odot$ star 12 parsecs away (Gillon et al. 2016). Subsequent monitoring with the *Spitzer Space Telescope* uncovered an additional four planets (Gillon et al. 2017). This system has already been studied with *HST* in order to begin obtaining an atmospheric transmission spectrum (de Wit et al. 2016) and is a high priority target for observations with *JWST* (Barstow & Irwin 2016).

The MEarth Project is a photometric survey of mid-to-late M dwarfs estimated to be within 33 pc of the Sun. MEarth aims to detect low-mass rocky planets transiting these stars (Nutzman & Charbonneau 2008; Irwin et al. 2015). MEarth has announced the discovery of three planets, GJ 1214b (Charbonneau et al. 2009), GJ 1132b (Berta-Thompson et al. 2015), and a temperature super-Earth, LHS 1140b (Dittmann et al. 2017). GJ 1214b has been intensely studied; atmospheric characterization has been performed from optical wavelengths (Bean et al. 2011; Murgas et al. 2012; de Mooij et al. 2013) to the infrared (e.g., Bean et al. 2011; Croll et al. 2011; Crossfield et al. 2011; Désert et al. 2011; Berta et al. 2012a; Fraine et al. 2013; Kreidberg et al. 2014). Additionally, dedicated, long

---

duration, point-and-stare observations have been performed with the *Spitzer Space Telescope* in order to search for additional transit planets at periods of 20 days or less (Gillon et al. 2014). These observations did not uncover the existence of another planet in the GJ 1214 system.

Recently, MEarth discovered GJ 1132b, a rocky planet similar in size to the Earth in a 1.6 day orbit around a 0.181 $M_\odot$ star 12 parsecs from the Sun (Berta-Thompson et al. 2015). At this distance, atmospheric characterization with *HST* and *JWST* is feasible. With four orbits of *HST*, low mean molecular weight atmospheres without high-altitude aerosols are detectable. Secondary atmospheres consisting of heavier molecules such as O_2 or CO_2 require significant investments of observing time ($\approx$60 orbits of *HST*) to be detected. GJ 1132b's equilibrium temperature (400 K with a Venus-like albedo of 0.75) makes it unlikely to be habitable, but understanding whether its atmosphere is a primordial or secondary atmosphere can shed light on its formation and migration history and provide key insights into the nature of small planets around M dwarf stars (Schaefer et al. 2016). If additional transiting planets were to be found in this system, then these would also be valuable targets to perform atmospheric transmission spectroscopy measurements and enable comparative planetology studies to determine under what conditions atmospheres are likely to be primordial or secondary in origin. Our current understanding of exoplanetary systems allows us to assess whether such a search is likely to yield additional planets.

Data from the *Kepler* mission has shed light on the population of exoplanets. Muirhead et al. (2015) estimated that 21^{+7}_{-5}% of mid-M dwarfs host multiple planets, all with orbital periods less than 10 days. Assuming a disk mass-to-stellar mass ratio of 1%, these planets would account for nearly all of the non-hydrogen and helium disk mass, and Muirhead et al. (2015) suggest that this may indicate a very high efficiency in the planet formation mechanism around M dwarfs and a *lack* of planets at large orbital periods around mid-M dwarfs. A study by Ballard & Johnson (2016) generated synthetic populations of exoplanets described by a range of planet multiplicity and mutual inclination for comparison to the *Kepler* M dwarf sample. They found that the total number of single transiting planet systems is incompatible with the number of systems with multiple transiting planets, assuming a single planet population distribution. Instead, half of all M dwarf planetary systems consist of a single planet, while half of M dwarf systems contain five or more planets with a low mutual inclination (Ballard & Johnson 2016). If GJ 1132 harbors additional planets, we can attempt to uncover them via transit and radial velocity observations.

Here, we describe observations of the GJ 1132 system taken with the MEarth Observatory and the *Spitzer Space Telescope*. We have collected 21 transit observations with MEarth in our red optical bandpass and have observed for 100 near-continuous hours with *Spitzer*, collecting two transits. We seek to probe the GJ 1132 system for signs of additional transiting bodies in the system, including moons orbiting GJ 1132b and additional planets. In Section 2, we describe the observations from MEarth-South and from *Spitzer*. In Section 3, we describe our data analysis techniques and modeling the transit light curves of GJ 1132b. In Section 4, we discuss the photometric precision of our *Spitzer* data set and our sensitivity to additional transiting bodies.

2. Observations and Production of the Time Series

2.1. MEarth-South

MEarth-South consists of eight $f/9$ 40 cm Ritchey–Chrétien telescopes on German equatorial mounts situated at Cerro Tololo International Observatory (CTIO) in Chile (Irwin et al. 2015). The telescopes are robotic and take data on every clear night. Each telescope has a 2048 × 2048 pixel CCD, with a pixel scale of approximately $0\rlap{.}{''}84$ pix^{-1}. We use a Schott RG715 glass filter with an anti-reflection coating, which has a broadband red optical throughput. Each CCD is an e2v CCD230-42 device with an interference coating matched to our bandpass, which has the effect of reducing fringing. The CCDs operate at $-30°$C. Prior to each exposure we pre-flash the detector to eliminate persistence from the previous exposure. This increases the dark current in the CCD, which we subsequently subtract off in image processing.

We gather sky flat frames at dawn and at dusk each night. Because MEarth uses German equatorial mounts, we must rotate the field-of-view of the detector by 180° relative to the sky when crossing the meridian. Therefore, we take two sets of flat fields each at dawn and at dusk, taking adjacent pairs of flat fields on opposite sides of the meridian. These flats allow us to average out large-scale illumination gradients from the Sun and the Moon. Scattered light in our telescopes concentrates in the center of the field-of-view with an amplitude of approximately 5% of the average value of the sky across the CCD. To correct for the scattered light, we filter out large-scale structure in the background from our combined twilight flat field and use the residual flat field to track small scale features (inter-pixel sensitivity and dust shadows). The large-scale flat field is derived from dithered photometry of dense star fields.

We measure the nonlinearity of the MEarth detectors with a dedicated sequence of dome flats. The nonlinearity of the detectors is approximately 1%–2% at half the detector full well and rises to 3%–4% near saturation. We correct for this nonlinearity as part of the general MEarth pipeline, and all exposure times are set to avoid surpassing 50% of the full well.

In order to reach the precisions necessary to detect exoplanetary transits, we must measure and correct for the effects of differential color extinction due to the atmosphere. Changes in the amount of precipitable water vapor in the atmosphere over the course of an observing night result in changes in the atmospheric transmission in the red end of the MEarth bandpass. Because the MEarth targets are, by their nature as mid-to-late M dwarfs, the reddest objects in the field, these effects can produce systematic effects when using bluer stars as reference stars, as our target stars are more sensitive to the changes in the precipitable water vapor than are the field reference stars. We correct for these effects by measuring a "common mode" for all of our target M dwarfs. The common mode is the measure of the average differential light curve of all M dwarfs currently being observed by MEarth-South, in time bins of 0.02 days (28.8 minutes). This correlated behavior between targets is a good proxy of the local changes in precipitable water vapor through the night. In order to measure this common mode, half of the MEarth-South telescopes must be observing other M dwarfs during dedicated transit observations. Therefore, for each observed transit presented here, either 3 or 4 of the MEarth-South telescopes are observing GJ 1132; the rest are observing other M dwarfs to determine the common mode. We targeted all transits of GJ

1132b visible from CTIO between 2015 November 05 and 2016 July 05 civil date. We observed a total of 21 transits with 6 different telescopes over this time period and obtained 34,968 data points (we also observed some partial transits, but they are not included in this analysis).

We measure the position of the target and reference stars on each frame using a modified method from Irwin (1985). We bin each image into 64 × 64 pixel blocks and measure the peak of the histogram of the intensity of these super-pixels as an estimate of the local sky background. This process eliminates large-scale illumination gradients in image background. We estimate the sky background around each star with a sky annulus between 18 and 24 pixels away from the stellar photocenter. The photocenter of each star is determined from the intensity weighted first moment (the centroid) of the star.

We measure the total flux using a 6 pixel (≈5″04) or 8 pixel (≈6″72) aperture radius, depending on the seeing conditions of the individual night and adopt an aperture correction to correct for the stellar flux that lies outside of the aperture. The aperture correction varies from night to night with atmospheric conditions but has a typical value around 0.04 mag. As we are performing relative photometry for this analysis, the aperture corrections of the target star and the reference stars cancel out. Pixels that are partially within the circular aperture are weighted by the fraction of the pixel that would lie within an idealized circular aperture at the stellar location.

Each transit observation from each telescope is reduced independently of the others, although the common mode is common to all telescopes. Each light curve out-of-transit baseline is normalized to 1.0 and we fit a linear term times the common mode to the time series to remove trends due to the atmosphere in the data. We vary each eclipse normalization in our light curve analysis, but we do not vary GJ 1132's coupling constant to the common mode during our analysis.

2.2. Spitzer

Spitzer obtained data with the Infrared Array Camera at 4.5 μm as program 12082 (PI Dittmann). We obtained 100 hr of nearly continuous *Spitzer* observations, beginning on 2016 April 24 and ending on 2016 April 28 UT. Observations spanned from BJD 2457502.0064004 to 2457506.3296307. During this span, there were seven breaks in the data longer than 10 s in duration. The largest, between BJD 2457503.4590452 and 2457503.6895174 (approximately 5.5 hr), was due to a data downlink.

Our program was divided into six Astronomical Observation Requests (AORs). The duration of these AORs were 20 hr, 14 hr, 20 hr, 20 hr, 15 hr, and 8 hr. Between each AOR there was a gap of 12–250 s with the 5.5-hr downlink occurring at the end of the 14-hr AOR. This data set consists of 2725 sets of 64 individual subarray images with an integration time of 2 s, for a total of 174,400 total data points. We obtained data with the subarray mode, placing GJ 1132 in the portion of the detector that is well characterized for the purpose of obtaining high precision light curves. In order to improve cadence and have a reasonable data volume, we utilized a small 16 × 16 pixel portion of the detector. These data were calibrated with the *Spitzer* pipeline version S19.2.0, and the timestamps of each data point are calculated at the solar system barycenter.

We correct our *Spitzer* data with the pixel-level decorrelation (PLD) method, described by Deming et al. (2015). The approach of the PLD reduction method is that it uses the brightness values encoded on the pixels themselves instead of correlating brightness fluctuations with a measure of the location of the star on the CCD (which itself depends on the pixel values). Due to the pointing stability of *Spitzer*, the location of the stellar image does not drift significantly, even over observations lasting several hours. The 50th percentile of the photocenter difference from the median photocenter in each AOR is 0.062 pixels. The 95th percentile for the difference in the photocenter from its median location is 0.126 pixels. At the beginning of each AOR, the target falls on a slightly different location of the array, but the photocenter remains stable within each AOR. This pointing stability and the relatively large size of the *Spitzer* point-spread function allow us to describe the instrument-based variations in the light curve from image motion and pixel sensitivity as a linear combination of the pixels in the image themselves.

We select a 5 × 5 pixel area centered on the center pixel of the subarray encompassing the flux from GJ 1132. We sum the pixels in this square area in order to obtain the total brightness in this aperture and then divide each pixel by this value in order to normalize each pixel to this value. We do this for each of the 174,400 images. Deming et al. (2015) note that binning the data prior to fitting pixel coefficients can provide better stability on timescales relevant for planetary transits in exchange for poorer stability on shorter (several second) timescales. Binning data allows us to better determine the pixel coefficients at the edge of the aperture, where the flux is low in any individual 2 s exposure. We bin our data into 60 s blocks for the purposes of fitting our model coefficients. We note that because this method involves normalizing the pixel values as a percentage of the total flux, it removes astrophysical variations (i.e., the transit) from this normalization procedure, while allowing variations due to pixel sensitivity, flat fielding error, and image motion to be calibrated out via the relative values of each pixel coefficient.

We fit the following model:

$$F_i = \sum_{n=1}^{25} C_n P_{n,i} + b \qquad (1)$$

where F_i is the total flux at time i, n is the pixel number (of the 25 pixels in the model), C_n is the coefficient for each pixel, $P_{n,i}$ is the normalized value of pixel n at time i, and b is a constant. As the pixel values are normalized and for the purpose of this model, the variations in F_i are assumed to be due to the flux from individual pixels shifting to adjacent pixels as the photocenter shifts during the observation.

Deming et al. (2015) also included a linear and a quadratic term in time in their model, but we omit those terms here as we find them to be insignificant for our data set. When fitting this model, we eliminate any data points where the total unnormalized flux is more than 3σ discrepant from the median across the AOR. Because we are seeking to obtain only the coefficients for each pixel, this will mitigate the potential influence of individual outliers. We also exclude all in-transit data points from this analysis, although a reduction including these data points does not significantly affect our results, and therefore we do not think that this data reduction method can suppress potential transit signals from other bodies in the system. This is because the pixels are normalized for each time stamp, so real astrophysical variations are eliminated. The only way for this reduction method to suppress real astrophysical

Table 1
Photometry of GJ 1132

Time (BJD)	Flux	Error	Instrument
2457332.742537	0.9917	0.0053	MEarth
2457332.743049	1.0053	0.0052	MEarth
2457332.743572	0.9997	0.0052	MEarth
2457332.744091	1.0064	0.0052	MEarth
2457332.744603	0.9937	0.0051	MEarth

(This table is available in its entirety in machine-readable form.)

Table 2
Transit Model Parameters

Parameter	Prior
$\frac{a}{R_*}$	Uniform [12, 20]
i	Uniform [85, 90]
$\frac{R_p}{R_*}$	Uniform [0.0362, 0.0662]
P	Uniform [1.628744, 1.629116]
T_0	Uniform [2457184.55594, 2457184.55978]
$a_{4.5}$	Uniform [0.2496, 0.3744]
$b_{4.5}$	Uniform [0.1270, 0.1904]
a_{MEarth}	Uniform [0.1702, 0.2554]
b_{MEarth}	Uniform [0.3206, 0.4808]

Note. $\frac{a}{R_*}$ is the ratio of orbital semimajor axis and stellar radius. i is the orbital inclination angle in the plane of the sky in degrees. $\frac{R_p}{R_*}$ is the ratio of planetary radius and stellar radius. P is the orbital period in days. T_0 is the transit epoch (BJD). $a_{4.5}$ and $b_{4.5}$ are the quadratic limb darkening coefficients in *Spitzer* Channel 2. a_{MEarth} and b_{MEarth} are the quadratic limb darkening coefficients in the MEarth-South bandpass.

variations is if they are directly correlated with shifts of the stellar photocenter. We fit each of our six individual AORs independently. The pixel coefficients can change by as much as 50% due to the new average location of the photocenter with each repointing.

Once we obtain the pixel coefficients for each individual AOR, we apply these coefficients to the *unnormalized* pixel-level data and sum the data in these pixels in order to obtain the flux of GJ 1132. All data that was omitted for the purpose of fitting the pixel coefficients is reinstated for the purpose of measuring the light curve. We apply a new outlier rejection method to these data. For each individual data point, we measure the median flux value within a ±10-minute window of that data point as well as the median absolute deviation from the median (MAD, Hoaglin et al. 1983) in this window. If the data point is more than 10 MADs discrepant from the local median value, it is discarded; 169 of 174,400 data points are discarded due to this criterion. None of these excluded data points occurs within 10 minutes of each other, and therefore we believe these to be outliers and not indicative of short timescale astrophysical variability.

In Table 1, we provide the corrected photometry for GJ 1132 for all eclipses taken with MEarth-South and *Spitzer*.

3. Modeling of the Time Series

We obtained observations of 21 transits in the near red optical *MEarth* filter and 2 transits in the *Spitzer* 4.5 μm channel. Each MEarth transit contains both pre-transit and post-transit data for the purpose of establishing an out-of-transit baseline, while the *Spitzer* data set includes approximately 98 hr of out-of-transit observations. We fit our observations with the `batman` code (Kreidberg 2015), which is an an optimized python implementation of the Mandel & Agol (2002) analytic model for transit light curves. In Table 2, we describe the parameters of the model we use to fit our transit observations.

We initiate our model with the physical parameters found in Berta-Thompson et al. (2015). We adopt limb darkening coefficients from Claret et al. (2012) for a 3300 K star with a log(*g*) = 5.0 and a solar metallicity. We adopt the limb darkening coefficients for a Cousins *I*-filter for our MEarth observations, as the effective wavelength is similar. For our *Spitzer* data, we adopt limb darkening parameters from Claret et al. (2013), which are calculated for the *Spitzer* bandpass. We note that while GJ 1132 is slightly metal-poor, we adopt solar metallicity limb darkening parameters. However, we allow significant variation in the limb darkening parameters via our priors in order to allow our model to adapt to slightly different limb darkening laws due to the stellar metallicity and the slightly different stellar type compared to Claret et al. (2012).

Due to the large quantity of data compared to the initial discovery observations, we adopt very loose priors for our model. For our priors, we let each parameter vary freely with no penalty within 5σ of the values determined by Berta-Thompson et al. (2015). We let limb darkening coefficients vary freely (uniform prior) within 20% of their initial value from Claret et al. (2012), to account for slight differences between GJ 1132 and the stellar models as well as for differences in the effective bandpass between the *MEarth* and the Cousins *I*-filter. We fix the eccentricity of GJ 1132b to zero. Fixing the eccentricity to zero may bias the stellar density measured from the light curve (Carter et al. 2011). However, the short period of GJ 1132b implies that the eccentricity is either zero or very low due to tidal forces (circularization timescale of approximately 400,000 years; see, e.g., Berta-Thompson et al. 2015) and would have little effect on our measurement. The radial velocity measurements obtained by Berta-Thompson et al. (2015) were unable to provide a robust constraint on eccentricity. Our priors do not significantly affect our result, as the parameters in our chain do not vary to the edges of our priors and so are not "cut-off" by them.

In order to explore the parameter space, we use the `emcee` code (Foreman-Mackey et al. 2013), a python implementation of the Affine Invariant Markov Chain Monte Carlo sampler. We allow the ratio of the radii to vary between the different bandpasses. This allows us to probe the effect of unoccluded starspots (which will more strongly affect the red optical MEarth data than the longer wavelength *Spitzer* data), as well as begin to probe the transmission spectrum of GJ 1132b's atmosphere.

Each model is initiated with 100 walkers in a Gaussian ball located at the initial solution described above. We run each chain for 75,000 steps and discard the first 10% of the resultant samples so that the solution may "burn-in" irrespective of the initialization. This burn-in appears to occur earlier than this cut-off for all parameters in the model, but we retain this 10% cut-off to avoid any possible systematics. We report the best-fit model from this chain, as well as the 16th and 84th percentile for each parameter in Table 3. In Figure 1, we show the transit data collected by MEarth and *Spitzer* as well as our best-fitting model, and in Figure 2 we show the transits observed by

Table 3
System Parameters

Parameter	Value	Source
$\frac{a}{R_*}$	$16.54^{+0.63}_{-0.71}$	This work
i (degrees)	$88.68^{+0.40}_{-0.33}$	This work
$\frac{R_p}{R_*}$ (Spitzer)	0.0492 ± 0.0008	This work
$\frac{R_p}{R_*}$ (MEarth)	0.0455 ± 0.0006	This work
P (days)	$1.6289246^{+0.0000024}_{-0.0000030}$	This work
T_0 (BJD)	$2457184.55804^{+0.00054}_{-0.00039}$	This work
$a_{4.5}$	$0.313^{+0.0041}_{-0.0042}$	This work
$b_{4.5}$	$0.154^{+0.022}_{-0.018}$	This work
a_{MEarth}	$0.215^{+0.016}_{-0.027}$	This work
b_{MEarth}	$0.407^{+0.049}_{-0.064}$	This work
Derived Parameters		
R_* ($R_\odot$)	$0.2105^{+0.0102}_{-0.0085}$	This work
ρ_* ($\rho_\odot$)	$19.4^{+2.6}_{-2.5}$	This work
M_* ($M_\odot$)	0.181 ± 0.019	Berta-Thompson et al. (2015)
M_p ($M_\oplus$)	1.62 ± 0.55	Berta-Thompson et al. (2015)
R_p ($R_\oplus$)	1.130 ± 0.056	This work
ρ_p (g cm^{-3})	6.2 ± 2.0	This work
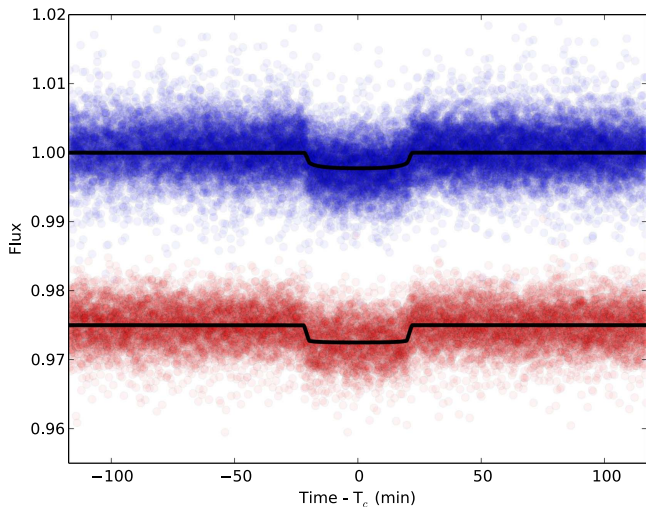
Figure 1. Stacked transit light curves of 21 transits from the MEarth Observatory (blue) and 2 transits from Spitzer (red, offset for clarity). The black line is our best model fit to the data. We find a slightly larger planet-to-star radius ratio in the MEarth red optical passband than in the 4.5 μm Spitzer passband, which we attribute to the effect of a combination of faculae and occulted starspots. We use these transit light curves to refine the orbital ephemeris of the planet, as well as resolve the ingress and egress times, placing stronger constraints on the radius of the star (and therefore the radius of the planet) than previously determined.

Spitzer, binned on 3-minute timescales along with the transits observed by MEarth. Our space-based Spitzer observations are more precise and have sufficient cadence to resolve the ingress and egress of the transit.

Additionally, with our best-fit transit model, we fit each transit individually solely for the best transit time, in order to potentially detect transit timing variations due to the presence of a perturbing body. We measure each individual transit time by holding our best-fit transit model constant and solely fitting the central time of transit. We construct an observed–calculated
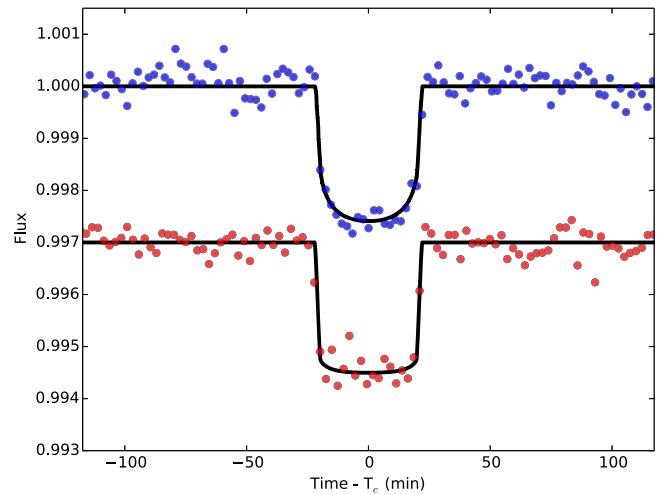

Figure 2. MEarth (blue) and Spitzer (red) observations of transits of GJ 1132b, binned on 3-minute timescales (90 data points per bin, for Spitzer), offset for clarity. We measure a transit depth of 2.42 ± 0.08 mmag. The high-cadence capabilities of Spitzer allow us to resolve the ingress and egress time, allowing us to more reliably measure the parameters of the system.
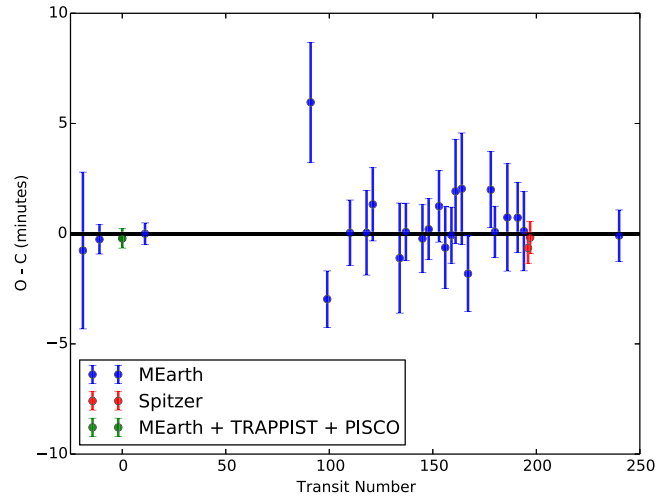

Figure 3. Observed–Calculated (OC) diagram for the transits presented in this paper. Blue data points represent measurements from MEarth-South, the green data point at epoch 0 is the measurement from a combination of MEarth-South, TRAPPIST, and PISCO data presented by Berta-Thompson et al. (2015), and the red data points represent the measurements from Spitzer. We measure the best-fitting individual transit time for each transit using our globally best-fitted transit model, varying only the central time of transit. We measure the difference between the transit time of each individual transit and the linear ephemeris from our best-fit model. We find no evidence of transit timing variations in this system, suggesting that any additional bodies in the GJ 1132 system are not in or near mean-motion resonances with GJ 1132b.

diagram (OC) showing the deviation of an individual transit time from the best-fit ephemeris, including the transits measured in the initial discovery observations in Berta-Thompson et al. (2015) (Figure 3), and provide our individual measured transit times in Table 4.

4. Discussion and Conclusion

Deming et al. (2015) demonstrated using Spitzer data taken of the M dwarf planetary host GJ 436 (Ballard et al. 2010) that they could recover near-to-photon-limited behavior down to a level of 100 ppm in 1000 s. We find a similar behavior for the PLD algorithm for our data set. In Figure 4, we show the

Table 4
Individual Transit Times

| Epoch	Transit Time (BJD)	Error	Instrument
−19	2457153.6079	0.0024	MEarth
−11	2457166.63969	0.00046	MEarth
0	2457184.55789	0.00031	MEarth + TRAPPIST + PISCO
11	2457202.47611	0.00034	MEarth
91	2457332.7943	0.0019	MEarth
99	2457345.81951	0.00089	MEarth
110	2457363.7397	0.0010	MEarth
118	2457376.7712	0.0013	MEarth
121	2457381.6588	0.0012	MEarth
134	2457402.8332	0.0017	MEarth
137	2457407.72076	0.00090	MEarth
145	2457420.7519	0.0011	MEarth
148	2457425.63902	0.00096	MEarth
153	2457433.7844	0.0011	MEarth
156	2457438.6698	0.0013	MEarth
159	2457443.55700	0.00088	MEarth
161	2457446.8162	0.0016	MEarth
164	2457451.7030	0.0018	MEarth
167	2457456.5872	0.0012	MEarth
178	2457474.5080	0.0012	MEarth
180	2457477.76452	0.00081	MEarth
186	2457487.5385	0.0017	MEarth
191	2457495.6831	0.0011	MEarth
194	2457500.5695	0.0013	MEarth
196	2457503.82680	0.00048	*Spitzer*
197	2457505.45606	0.00051	*Spitzer*
240	2457575.49988	0.00081	MEarth
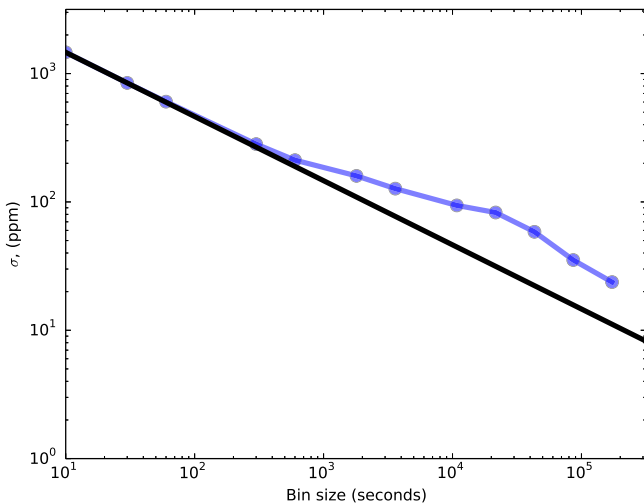
Figure 4. Standard deviation of the *Spitzer* 100-hr time series as a function of bin size. The black line is a line of slope −1/2 anchored to measured standard deviation in 10 s bins. We find that our *Spitzer* data and reduction technique follows the photon noise limit to a precision of 250 ppm, which we achieve at 10-minute bin sizes. We reach a photometric precision of 159 ppm in 30 minutes, which is slightly shorter than the duration of the transit of GJ 1132b and similar to the transit duration that would be expected for planets interior to GJ 1132b. For a 0.21 $R_\odot$ star and a 3σ detection of the transit depth, this corresponds to a body 94% the radius of Mars. We note that the extremely large bin sizes at the right end of the plot means that we are effectively calculating the difference in the average of a handful of bins.

standard deviation of our residuals from the *Spitzer* observations as a function of bin size. We find that our *Spitzer* data shows approximately photon-limited behavior for bin sizes of 10 minutes and smaller, for a precision of approximately 200 ppm. At larger bin sizes, we do not recover photon-limited

behavior, although the standard deviation of our residuals continues to decrease. On 30-minute timescales, we obtain a standard deviation of 160 ppm, for a 1σ transit precision equal to the size of Earth's moon.

4.1. The Stellar Radius of GJ 1132

Recent work by Southworth et al. (2017) has estimated a larger stellar radius for GJ 1132. Southworth et al. (2017) observed nine transits of GJ 1132b with the GROND instrument, which can observe simultaneously in *griz*, with a cadence of approximately 1–2 minutes (the cadence of their observations was not stated in their work). Using these light curves, they measure a stellar density of $10.9^{+3.4}_{-2.4}\rho_\odot$, approximately half of that found by Berta-Thompson et al. (2015). This density measurement is highly discrepant with the stellar densities of typical M dwarfs, and it inflates the inferred radius of GJ 1132 to $0.255 \pm 0.023\ R_\odot$ (Southworth et al. 2017). Determining stellar densities with transit light curves requires accurately resolving both the full transit duration as well as the ingress and egress durations. In the case of GJ 1132b, the ingress time is only a few minutes in duration, and so the cadence of both the GROND and MEarth instruments are ill-suited for resolving transit ingress and egress. To compound this cadence challenge, both MEarth and GROND must contend with the correlated and uncorrelated noise induced by the Earth's atmosphere, which are typically of the same size as the transit depth itself. Therefore, determining an accurate ingress and egress duration from the ground typically involves stacking multiple transit observations together, which require an ephemeris comparable in accuracy to the ingress and egress time and is still sensitive to systematics in the data.

With *Spitzer*, we are able to utilize a 2 s cadence observing strategy to resolve the ingress and egress duration of our individual transits. Furthermore, *Spitzer* is not affected by atmospheric effects and therefore can deliver a well-sampled and precise light curve from which to measure the ingress and egress. This allows us to directly measure the stellar density and resolve the discrepancy between Southworth et al. (2017) and Berta-Thompson et al. (2015). We find a stellar density of $19.4^{+2.6}_{-2.5}\rho_\odot$, consistent with the determination from Berta-Thompson et al. (2015) and with stellar models. We suggest that the unrealistically low stellar density inferred by Southworth et al. (2017) is likely due to uncorrected systematic effects in their data.

We use the stellar mass determined by Berta-Thompson et al. (2015), which relied on a trigonometric parallax from Jao et al. (2005) and the mass–luminosity relation of Delfosse et al. (2000), combined with our measurement of the stellar density to measure the radius of GJ 1132. We measure a stellar radius of $R = 0.2105^{+0.0102}_{-0.0085}\ R_\odot$, which is consistent with the value originally reported by Berta-Thompson et al. (2015), but inconsistent at 4.3σ with that reported by Southworth et al. (2017). We reiterate that this value may be biased by our assumption of zero eccentricity for the orbit of GJ 1132b (Carter et al. 2011), but believe that a 0 or negligible eccentricity is likely due to the close-in orbit of GJ 1132b. We use this measurement of the stellar radius as well as our measurement of the transit depth from the *Spitzer* light curves, which are less affected by the effects of starspots, to measure a planetary radius of $1.130 \pm 0.056\ R_\oplus$, consistent with but more precise than the value determined by Berta-Thompson et al. (2015). We note that the $1.43 \pm 0.16\ R_\oplus$ radius reported by

Southworth et al. (2017) is due primarily to their measurement of the stellar density and radius and not from their measurement of the transit depth.

4.2. The Optical and Infrared Transit Depths of GJ 1132b

Our best-fit measurement for the ratio of the planetary and stellar radii is $\frac{R_p}{R_*} = 0.0455 \pm 0.0006$ in the MEarth bandpass and $\frac{R_p}{R_*} = 0.0492 \pm 0.0008$ in the *Spitzer* 4.5 μm channel. The MEarth bandpass, being bluer, is more sensitive to the effects of starspots on the star. While GJ 1132 is a photospherically quiet star, some magnetic activity and starspots exist on its surface, as we have been able to measure rotational modulation due to the longitudinally asymmetric distribution of these spots (Berta-Thompson et al. 2015). Unfortunately, because this rotational modulation is sensitive only to the longitudinally asymmetric component of the starspot distribution, the stellar sinusoid is not effective in constraining what we might expect in a transit depth measurement from the sinusoidal phase alone, as there is likely to be a symmetrically distributed component to the stellar starspots as well as latitudinal asymmetries that we are not sensitive to. In order to reconcile the difference between the observed transit depth in MEarth and *Spitzer*, GJ 1132b's transit chord could lie along an active stellar latitude. For a starspot that is completely dark in the MEarth bandpass compared to the non-spotted stellar surface, GJ 1132b must occult a starspot only 1500 km in radius in order to account for the observed transit depth difference. For a starspot with an effective temperature 0.7 times the effective temperature of the non-spotted photosphere, the starspot size required increases to 3000 km. This is consistent with the starspot size distribution of NGC 2516, although there are significant degeneracies between starspot size, starspot filling fraction, and the starspot to photosphere temperature ratio (Jackson & Jeffries 2013). However, we do not see discrete star-crossing events (such as those seen in TrES-1b; e.g., Dittmann et al. 2009), although the precision of the MEarth light curves would make these difficult to identify. We believe that the effects of planetary starspot occultation can explain the difference between these two radii measurements and are not due to a broad spectral feature in GJ 1132b's atmospheres, which would require a scale height 540 km deeper in the blue MEarth bandpass than at the *Spitzer* 4.5 μm bandpass.

Alternatively, recent work by Rackham et al. (2017) have suggested that the presence of starspots may only be a secondary effect modulating the transit depth. They suggest that the presence of unoccluded bright regions (faculae) have a greater effect on the transit depth. They find, for the GJ 1214 system (a similar system to GJ 1132), that the planet-to-star radius ratio is shallower at optical wavelengths than at near-infrared wavelengths, similar to the results we find for GJ 1132b. In order to reconcile those results, Rackham et al. (2017) determine that only 3.2% surface coverage by faculae with a temperature difference of approximately 350 K is needed in order to increase the apparent size of GJ 1214b by 0.05 $R_\oplus$. We find a difference between the size of GJ 1132b at optical and infrared wavelengths of approximately $0.085 \pm 0.023 R_\oplus$ (3.7σ significance), similar in magnitude to the difference seen in GJ 1214b transit depths. We therefore believe that this is also a plausible explanation for the differences in our transit depth measurements. Because GJ 1132b is known to be magnetically active, likely some effects of unoccluded spots and faculae are
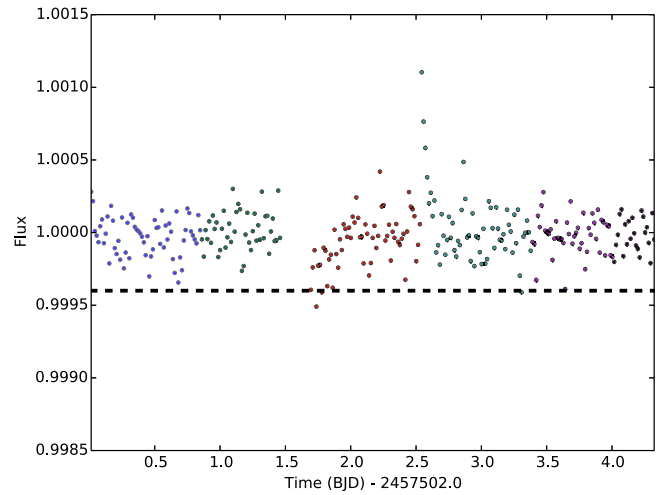

Figure 5. Flux of GJ 1132 with transits of GJ 1132b removed (residuals are shown) for the 100-hr *Spitzer* campaign. Each color represents a new AOR, where a *Spitzer* repointing occurred. We have binned the data on 20-minute timescales. We reach a photometric precision of 159 ppm in 30 minutes (35% shorter than the transits of GJ 1132b). With this precision, we would detect the transits of a body the size of Mars with 3σ confidence (shown as black dashed line). We note that a transit would occur over multiple consecutive bins, and that while individual bins cross this threshold, we do not detect a transit-like event. These negative outliers are at the start of an AOR after the Earth-pointing data downlink are likely due to thermal systematics from the data downlink and the large change in spacecraft orientation and are unlikely to be astrophysical in origin (see Section 4.6). The brightening event visible at BJD 2457504.5 occurs at the beginning of an AOR, and we think it is likely to be a systematic effect and not due to a flare from the host star.

unaccounted for in our analysis and will complicate future atmospheric studies of planets around even mildly active M dwarfs.

4.3. Limits on Single-transit Events from Other Bodies

The observations presented here contain 100 hr of observations in a 105-hr window, with the only significant gap in observations occurring during an Earth data downlink. We find an orbital inclination of $88.68^{+0.40}_{-0.33}$ degrees for GJ 1132b. Assuming coplanarity, additional planets in the system would also transit GJ 1132 out to a period of 6.9 days, longer than the observations presented here. Therefore, if any coplanar planetary bodies exist in the GJ 1132 system with periods of 4 days or less, we should see them transit during our set of observations. Between 4.17 days (100 hr) and 6.9 days, our sensitivity decreases due to the increasing probability that a potential transit falls outside of the *Spitzer* window of observations. At periods longer than 6.9 days, coplanar objects can still transit, but this requires a nonzero eccentricity or alignment of the line of nodes.

In Figure 5, we show the flux of GJ 1132 at 4.5 μm during the entirety of the *Spitzer* campaign, binned on 20-minute timescales (roughly half the duration of a transit), with transits of GJ 1132b subtracted with our best-fitting transit model (residuals from this fit are shown). While there are no obvious transits of large bodies visible in this data set, we attempt to assess our sensitivity to single transits using the observed standard deviation of our data set on timescales relevant to exoplanetary transits. In Figure 4, we show that we can recover photon-limited behavior to a timescale of 10 minutes, at 200 ppm precision. In order to identify possible in-transit events, we bin our data to 10-minute timescales and search for
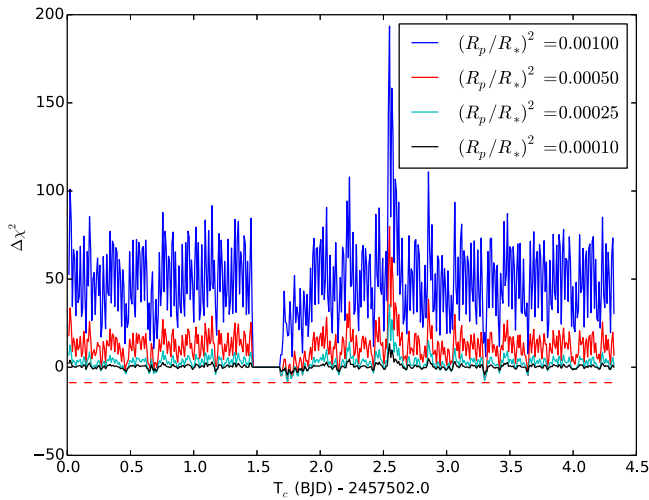
Figure 6. $\Delta\chi^2$ vs. central transit time for box-model transits compared to GJ 1132b-only models. Negative $\Delta\chi^2$ indicate a better fit to the data. The lower values after the data downlink are due to systematic effects associated with the data downlink, while the large spike around 2457504.5 BJD is due to a systematic associated with a repointing events. We find no significant box-like transit signals in this data set and can exclude signals belonging to a body $0.85 \times$ the size of Mars and larger. The approximate $\Delta\chi^2$ we would expect from the transit of a body $0.85 \times$ the size of Mars is indicated by the dashed red line.

Figure 7. Signal Residue (SR) as a function of orbital frequency for our 100 hr *Spitzer* program. We subtract the best-fitting transit model for GJ 1132b ($P = 1.6289246^{+0.0000024}_{-0.0000030}$ days) and use the box least square algorithm from Kovács et al. (2002) to compute the best-fitting box signal at each orbital period. We find no significant signals at short periods ($P < 50$ hr). The broad peak located near $P = 0.3$ days (frequency = 3.3) is associated with the large positive flux deviation at 2457504.5 BJD and additional positive outliers in the data set. Individual peaks in this diagram are also due to this large positive flux deviation. We find no significant periodic negative flux deviation signal in our data set and exclude transits approximately three quarters the size of Mars at periods of 50 hr or less.

any negative outlier detected at 3σ, corresponding to a sensitivity to bodies the size of Mars. We have 590 data bins. With white noise fluctuations alone, we would expect 1.8 3σ outliers, half of which would be negative outliers. Because a transit signal is likely to extend for greater than 10 minutes in duration, we would expect any significant transit signal to span more than one consecutive bin. We find three negative outliers with greater than 3σ significance, two of which we believe to be due to transient thermal effects from *Spitzer* data downlink and repointing (see Section 4.6).

We estimate the minimum radius transiting body we can exclude with this data set by comparing the χ^2 of our transit model with solely GJ 1132b and a model that includes a box-model transit of another body. We choose a box width of 40 minutes, which is a similar timescale to that we would expect from a transiting body. We vary the depth of the box in order to assess our sensitivity to other bodies. In Figure 6, we plot the $\Delta\chi^2$ from box models of varying transit depth and choice of central transit time when compared to our GJ 1132b-only model. Better fits to the data have a negative $\Delta\chi^2$. We find that that we can exclude transiting bodies 0.85 times the size of Mars or larger with an orbital period of 100 hr or less. This observation also excludes 60% of the orbit of bodies located at 6.9-day orbital periods (the maximum period a coplanar object with zero eccentricity would still transit the host star). Smaller bodies are permitted, as they do not significantly change the χ^2, but we see no evidence for them in this data set. Because this data also spans the times around the transits of GJ 1132b, we can also exclude exomoons around GJ 1132b to this same size. However, we note that due to the proximity of GJ 1132b to its host star, the hill sphere of GJ 1132b overlaps with the Roche lobe. Therefore, exomoons are not dynamically stable around GJ 1132b and we do not expect any to exist.
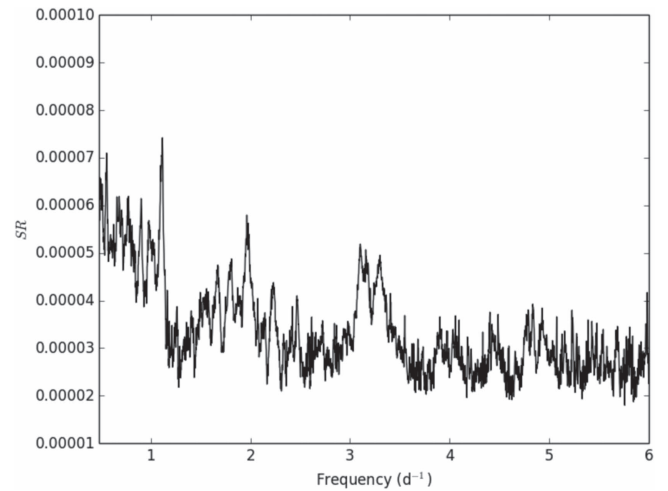
4.4. Limits on Extremely Short Period Bodies

Transiting bodies with orbital periods of 50 hr or less would show multiple transits during the span of our observation. With multiple transit measurements, we can increase our sensitivity to small bodies, provided we can search over the required period-space in order to coherently stack the transits together. In order to search for the presence of transiting bodies on ultra short periods, we first subtract the best-fitting transits of GJ 1132b from our *Spitzer* data set. We searched for periodic signals using the box least squares (BLS) method described by Kovács et al. (2002). We plot the signal residue as a function of orbital frequency in Figure 7. The broad signal located approximately at a period of 0.3 days is associated with positive flux outliers in the our data and not possible transit signals. The best-fit "depth" for this signal is -0.0002 (i.e., a brightening) of the total flux. We can exclude bodies the size of 0.74 times the size of Mars in orbital periods of 50 hr or less. We note that this limit is larger than the limit expected from stacking transits with Poisson noise due to red noise in our *Spitzer* light curve at large timescales.

4.5. Limits on Additional Bodies from Transit Timing Variations

We see no significant deviations from a linear ephemeris from any of the measured central transit times. Our observations span 259 epochs, or 422 days. Only one observation is more than 5 minutes deviant from a linear ephemeris, and this observation has an error bar of 2.7 minutes due to the relatively poorer weather conditions during this observation. Transit timing variations are largest (and most detectable) when the perturbing body is near a first-order mean-motion resonance (Holman & Murray 2005), although perturbations from bodies in a second-order resonance are also detectable (Deck & Agol 2016). Planets
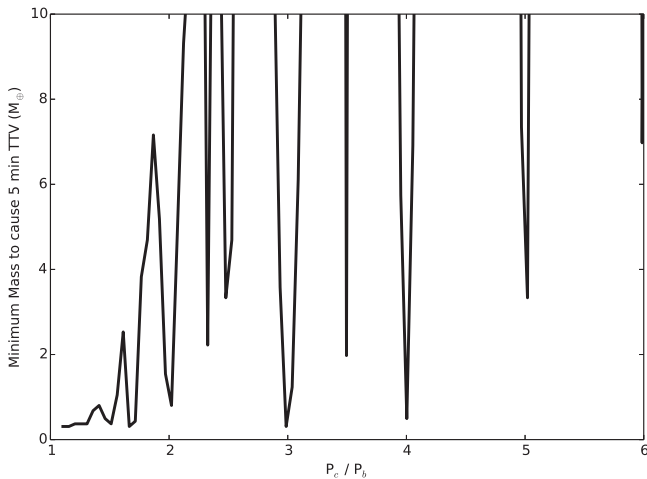
Figure 8. Minimum mass vs. Period ratio for our TTV simulations with TTVFast. Here, we assess the minimum perturbing mass needed in order to induce a TTV signal of 5 minutes or more in a single transit over 500 days. We find that close to the orbital period of GJ 1132b, small (and likely unstable) perturbers are necessary to cause a deviation, but beyond a period ratio of 2:1, our TTV non-detection is only sensitive in ruling out planets near mean-motion resonances. For the 2:1, 3:1, and 4:1 mean-motion resonances, we can rule out companions with masses less than that of Earth.

Period ratio (P_c/P_b)	Minimum Mass ($M_\oplus$)
1.50	0.37
1.66	0.31
2.02	0.80
2.32	2.22
2.48	3.33
2.99	0.31
3.49	1.98
4.00	0.49
5.02	3.33
5.99	6.97

in retrograde orbits relative to the planet whose transit times are being measured also show diminished amplitudes, further restricting the sensitivity of a TTV analysis to placing upper limits on additional planetary bodies in a system (Payne et al. 2010). We see no evidence for any transit timing variations over this timescale, and therefore conclude that it is unlikely any bodies of significant mass exist near mean-motion resonances with GJ 1132b.

In order to assess what mass bodies we may exclude with our current transit timing data, we use the TTVFast code (Deck et al. 2014). We initiate our TTVFast models with GJ 1132b in a circular orbit with our best-fitting values as derived in our photometric analysis. We initiate our perturbing planet with a random eccentricity uniformly distributed between 0.0 and 0.1, with an inclination randomly and uniformly distributed within 20° of the orbital plane of GJ 1132b. The longitudinal node, mean anomaly, and argument of pericenter of the perturbing planet are selected randomly. The mass of the perturbing planet is initiated at one-fifth the mass of GJ 1132b. We run TTVFast for 500 days and record the transit times of the inner planet. We fit a linear ephemeris to these simulated transit times and record the largest individual TTV measured from this simulation. If no transit time is discrepant from a linear ephemeris by 5 minutes or more, we increase the mass of the perturber by one-tenth the mass of GJ 1132b and repeat the simulation until this condition is met. We repeat this analysis for periods between 1.8 and 10 days, and for each period assessed, we repeat this analysis (with different random eccentricities, inclinations, mean anomalies, longitudinal node, and argument of pericenter) 21 times and select the median perturbing mass from this set in order to marginalize over possible effects due to these parameters. In Figure 8, we plot the minimum mass of a perturber needed in order to induce a 5-minute or higher transit timing variation from a linear ephemeris in GJ 1132b. We find that our transit times are only sensitive to perturbing objects close to mean-motion resonances with GJ 1132b. However, for these mean-motion resonances, particularly the 2:1, 3:1, and 4:1 resonances, we are able to exclude objects smaller than the mass of the Earth. In

Table 5, we list the local minima in this diagram and the minimum mass planet that can be excluded from this TTV analysis.

4.6. The Dimming Event at BJD 57503.69

We see one significant outlier signal immediately after the large gap in our data after the *Spitzer* data downlink. The depth of this signal is 0.022% and lasts for the first 3.5 hr after data collection resumes. This signal does not correlate with instrumental systematics such as pointing stability, voltage, or current applied to the heater, or any of the temperature measurements on the *Spitzer* spacecraft during these observations. In other long *Spitzer* stares of exoplanet hosts (like GJ 1214), similar signals after data downlink events have not been observed (Gillon et al. 2014). If this signal is real, it must begin at some point during the data downlink, and so 3.5 hr is the minimum transit duration for this signal. For a transit crossing the equator of the star, this corresponds to an orbital velocity of approximately 22 km s^{-1} and an orbital period of nearly 180 days. We note that if this signal is real, this body cannot be coplanar with GJ 1132b. Considering this extremely long duration, the unlikely chance that a body in an orbit with a period of 180 days would transit during a 100-hr observation window, the unlikely chance that if such a body existed that it would transit, and that this signal is coincident after a *Spitzer* repointing after data downlink, we believe that this signal is not real and is likely to be due to a spacecraft systematic associated with the data downlink and repointing.

4.7. Limits on the Secondary Eclipse of GJ 1132b

Our observations also contain three observations of the time of secondary eclipses of GJ 1132b (assuming zero eccentricity). The thermal variation expected from GJ 1132b assuming zero albedo and a temperature equal to the equilibrium temperature is 8 ppm. This is much smaller than the sensitivity of our *Spitzer* data. GJ 1132b would need an effective temperature of approximately 700 K if emitting as a blackbody in order to be detectable in our data. However, we can rule out secondary eclipses from extended warm atmospheres with our *Spitzer* observations. In Figure 9, we show our *Spitzer* light curve phase folded to GJ 1132b's ephemeris and binned on 10-minute timescales. We find a 3σ upper limit of 480 ppm for the secondary eclipse depth. This assumes that the eccentricity of GJ 1132 is zero, which has not yet been measured. We note that if GJ 1132b was eccentric, our search for additional transiting bodies would also be sensitive to secondary eclipses from GJ 1132b regardless of GJ 1132b's eccentricity. As we
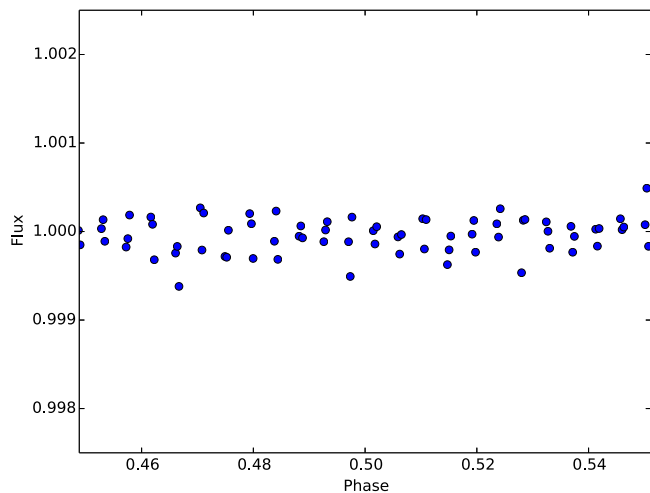
Figure 9. *Spitzer* observations phase folded to the ephemeris of GJ 1132b and binned on 10-minute timescales. We find no evidence for a secondary eclipse of GJ 1132b and rule out eclipse depths of 480 ppm at 3σ confidence. The expected secondary eclipse depth for GJ 1132b at the equilibrium temperature for its semimajor axis is approximately 8 ppm, and therefore these observations are not very constraining on the nature of GJ 1132b's atmosphere. In order to be detected in these observations, GJ 1132b would need to have a blackbody temperature of 700 K.

see no evidence for any additional transit signatures and cover the full phase of GJ 1132b's orbit, this upper limit for secondary eclipses is robust to assumptions about GJ 1132b's eccentricity.

4.8. Expectations for the GJ 1132 System from the Kepler Statistics

In this work, we have found no evidence for additional transiting bodies with periods of 100 hr or less. We further find no evidence for transit timing variations from bodies in mean-motion resonance with GJ 1132b. However, the *Kepler* dichotomy suggests that small rocky planets around M dwarfs (like GJ 1132b) are likely to host additional coplanar planets with periods less than 10 days, while single planetary systems (like GJ 436b and GJ 1214b) are more likely to be larger with significant gaseous envelopes. If GJ 1132 hosts additional planetary bodies, they must either be (a) smaller than the size of Mars such that any transits by these bodies would be undetected in our data, (b) mutually inclined with GJ 1132b such that they do not show a transiting geometry when viewed from the Earth, or (c), at orbital periods longer than 100 hr such that they did not transit during the timespan of our observations. Detecting bodies smaller than GJ 1132b, through either future transit measurements or RV measurements will be difficult, as the signal size is small. However, planets at longer period orbits can potentially be detected by future transit observations by, for example, TESS (if they transit), or through a sustained RV observational campaign if the mass of the planet is large enough to be detectable.

ORCID iDs

Jason A. Dittmann https://orcid.org/0000-0001-7730-2240
David Charbonneau https://orcid.org/0000-0002-9003-484X
Elisabeth R. Newton https://orcid.org/0000-0003-4150-841X

References

Ballard, S., Charbonneau, D., Deming, D., et al. 2010, PASP, 122, 1341
Ballard, S., & Johnson, J. A. 2016, ApJ, 816, 66
Barstow, J. K., & Irwin, P. G. J. 2016, MNRAS, 461, L92
Bean, J. L., Désert, J.-M., Kabath, P., et al. 2011, ApJ, 743, 92
Berta, Z. K., Charbonneau, D., Désert, J.-M., et al. 2012a, ApJ, 747, 35
Berta, Z. K., Irwin, J., Charbonneau, D., Burke, C. J., & Falco, E. E. 2012b, AJ, 144, 145
Berta-Thompson, Z. K., Irwin, J., Charbonneau, D., et al. 2015, Natur, 527, 204
Bonfils, X., Almenara, J. M., Jocou, L., et al. 2015, Proc. SPIE, 9605, 96051L
Buchhave, L. A., Dressing, C. D., Dumusque, X., et al. 2016, AJ, 152, 160
Carter, J. A., Winn, J. N., Holman, M. J., et al. 2011, ApJ, 730, 82
Charbonneau, D., Berta, Z. K., Irwin, J., et al. 2009, Natur, 462, 891
Claret, A., Hauschildt, P. H., & Witte, S. 2012, A&A, 546, A14
Claret, A., Hauschildt, P. H., & Witte, S. 2013, A&A, 552, A16
Croll, B., Albert, L., Jayawardhana, R., et al. 2011, ApJ, 736, 78
Crossfield, I. J. M., Barman, T., & Hansen, B. M. S. 2011, ApJ, 736, 132
de Mooij, E. J. W., Brogi, M., de Kok, R. J., et al. 2013, ApJ, 771, 109
de Wit, J., Wakeford, H. R., Gillon, M., et al. 2016, Natur, 537, 69
Deck, K. M., & Agol, E. 2016, ApJ, 821, 96
Deck, K. M., Agol, E., Holman, M. J., & Nesvorný, D. 2014, ApJ, 787, 132
Delfosse, X., Forveille, T., Ségransan, D., et al. 2000, A&A, 364, 217
Deming, D., Knutson, H., Kammer, J., et al. 2015, ApJ, 805, 132
Désert, J.-M., Bean, J., Miller-Ricci Kempton, E., et al. 2011, ApJL, 731, L40
Dittmann, J. A., Close, L. M., Green, E. M., & Fenwick, M. 2009, ApJ, 701, 756
Dittmann, J. A., Irwin, J. M., Charbonneau, D., et al. 2017, Natur, 544, 333
Dressing, C. D., & Charbonneau, D. 2015, ApJ, 807, 45
Dressing, C. D., Charbonneau, D., Dumusque, X., et al. 2015, ApJ, 800, 135
Foreman-Mackey, D., Hogg, D. W., Lang, D., & Goodman, J. 2013, PASP, 125, 306
Fraine, J. D., Deming, D., Gillon, M., et al. 2013, ApJ, 765, 127
Gillon, M., Demory, B.-O., Madhusudhan, N., et al. 2014, A&A, 563, A21
Gillon, M., Jehin, E., Lederer, S. M., et al. 2016, Natur, 533, 221
Gillon, M., Jehin, E., Magain, P., et al. 2011, in Detection and Dynamics of Transiting Exoplanets, ed. F. Bouchy, R. Díaz, & C. Moutou (Les Ulis: EDP Sciences), 06002
Gillon, M., Triaud, A. H. M. J., Demory, B.-O., et al. 2017, Natur, 542, 456
Henry, T. J., Jao, W.-C., Subasavage, J. P., et al. 2006, AJ, 132, 2360
Hoaglin, D. C., Mosteller, F., & Tukey, J. W. 1983, Understanding Robust and Exploratory Data Analysis (New York: Interscience)
Holman, M. J., & Murray, N. W. 2005, Sci, 307, 1288
Irwin, J. M., Berta-Thompson, Z. K., Charbonneau, D., et al. 2015, in Cambridge Workshop on Cool Stars, Stellar Systems, and the Sun 18, ed. G. T. van Belle & H. C. Harris (Cambridge: Cambridge Univ. Press), 767
Irwin, M. J. 1985, MNRAS, 214, 575
Jackson, R. J., & Jeffries, R. D. 2013, MNRAS, 431, 1883
Jao, W.-C., Henry, T. J., Subasavage, J. P., et al. 2005, AJ, 129, 1954

Kipping, D. M., Nesvorný, D., Buchhave, L. A., et al. 2014, ApJ, 784, 28
Kovács, G., Zucker, S., & Mazeh, T. 2002, A&A, 391, 369
Kreidberg, L. 2015, PASP, 127, 1161
Kreidberg, L., Bean, J. L., Désert, J.-M., et al. 2014, Natur, 505, 69
Mandel, K., & Agol, E. 2002, ApJL, 580, L171
Muirhead, P. S., Mann, A. W., Vanderburg, A., et al. 2015, ApJ, 801, 18
Murgas, F., Pallé, E., Cabrera-Lavers, A., et al. 2012, A&A, 544, A41
Nutzman, P., & Charbonneau, D. 2008, PASP, 120, 317
Payne, M. J., Ford, E. B., & Veras, D. 2010, ApJL, 712, L86

Rackham, B., Espinoza, N., Apai, D., et al. 2017, ApJ, 834, 151
Rogers, L. A. 2015, ApJ, 801, 41
Schaefer, L., Wordsworth, R. D., Berta-Thompson, Z., & Sasselov, D. 2016, ApJ, 829, 63
Schwieterman, E. W., Meadows, V. S., Domagal-Goldman, S. D., et al. 2016, ApJL, 819, L13
Southworth, J., Mancini, L., Madhusudhan, N., et al. 2017, AJ, 153, 191
Sozzetti, A., Bernagozzi, A., Bertolini, E., et al. 2014, in European Planetary Science Congress 2014, EPSC Abstracts, 9, EPSC2014-824